ACS APPLIED MATERIALS & INTERFACES

Research Article

www.acsami.org

Enhancing the Photocatalytic Hydrogen Evolution Performance of a Metal/Semiconductor Catalyst through Modulation of the Schottky Barrier Height by Controlling the Orientation of the Interface

Yang Liu,[†,§] Xin Gu,[†,§] Wen Qi,[†,‡] Hong Zhu,[*,†,‡] Hao Shan,[†] Wenlong Chen,[†] Peng Tao,[†] Chengyi Song,[†] Wen Shang,[†] Tao Deng,[*,†] and Jianbo Wu[*,†]

[†]State Key Laboratory of Metal Matrix Composites, School of Materials Science and Engineering and [‡]University of Michigan−Shanghai Jiao Tong University Joint Institute, Shanghai Jiao Tong University, 800 Dongchuan Road, Shanghai 200240, P. R. China

Supporting Information

ABSTRACT: Construction of a metal−semiconductor heterojunction is a promising method to improve heterogeneous photocatalysis for various reactions. Although the structure and photocatalytic performance of such a catalyst system have been extensively studied, few reports have demonstrated the effect of interface orientation at the metal−semiconductor junction on junction-barrier bending and the electronic transport properties. Here, we construct a Pt/PbS heterojunction, in which Pt nanoparticles are used as highly active catalysts and PbS nanocrystals (NCs) with well-controlled shapes are used as light-harvesting supports. Experimental results show that the photoelectrocatalytic activities of the Pt/PbS catalyst are strongly dependent on the contacting facets of PbS at the junction. Pt/octahedral PbS NCs with exposed PbS(111) facets show the highest photoinduced enhancement of hydrogen evolution reaction activity, which is ∼14.38 times higher than that of the ones with only PbS(100) facets (Pt/cubic PbS NCs). This enhancement can further be rationalized by the different energy barriers of the Pt/PbS Schottky junction due to the specific band structure and electron affinity, which is also confirmed by the calculations based on density functional theory. Therefore, controlling the contacting interfaces of a metal/semiconductor material may offer an effective approach to form the desired heterojunction for optimization of the catalytic performance.

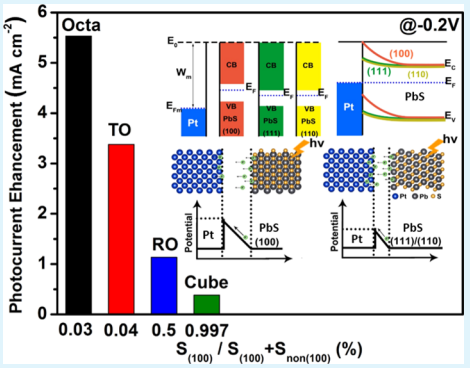

KEYWORDS: *photocatalysis, hydrogen evolution reaction, Schottky junction, energy bending, interface control*

1. INTRODUCTION

With the rapid development of modern society, it is imperative to search for new energy sources to replace traditional energy sources, such as fossil, gas, and coal. Among all kinds of renewable energy, solar energy can be exploited as an alternative to meet the ever-increasing needs due to its cleanliness and sustainability. However, solar-light harvesting must be coupled with efficient energy-storage mechanisms to maintain a constant energy supply during periods of low sunlight irradiation or at night.[1] Hydrogen can be used as an excellent energy carrier to store solar energy through water splitting because it can be utilized as an economic fuel to supply electric power whenever needed. Developing an efficient catalyst for the photoelectrochemical hydrogen evolution reaction (HER) as a part of water splitting is the key to constructing such sustainable and clean solar energy conversion systems.

It is well known that the most effective and widely used electrocatalytic HER catalysts are platinum (Pt) and Pt-based alloys, which facilitate HERs at low overpotentials to generate large cathodic current densities in the highly acidic solutions that are used for water electrolysis.[2] However, Pt-based HER catalysts are limited in their use for large-scale applications due to their scarcity and high cost . Many efforts have been devoted to developing earth-abundant, low-cost, and highly efficient HER catalysts through the development of bimetallic nanocrystals (NCs), with different structures and atomic distributions in the form of core-shells, alloys, and dendrites, by combining Pt with a secondary metal that is more abundant and/or less expensive, with an aim of overcoming the aforementioned limitations.[3−13] Previous studies have shown that some transition metal sulfides of tungsten, cobalt, nickel, iron, etc. are catalytically active in the HER.[14] Nonetheless, current studies are still not ready to be applied practically for hydrogen generation on a large scale.[8] Recently, a few works have focused on replacing the carbon support with semiconductors to construct a metal−semiconductor heterojunction to utilize solar energy to improve the electrocatalysis.[15,16] The

Received: January 29, 2017
Accepted: March 23, 2017
Published: March 23, 2017

DOI: 10.1021/acsami.7b01428
ACS Appl. Mater. Interfaces 2017, 9, 12494−12500

principle is that semiconductor NCs with exposed high-reactivity facets could generate charges to accelerate the charge-involving redox reactions, owing to the particular surface atomic arrangement and unsaturated dangling bonds in the cases of $BiVO_4$, Ag_3PO_4, Fe_2O_3, etc.[17−31] Li et al. studied the synergetic effect of dual cocatalysts deposited onto the different facets of $BiVO_4$ to construct highly efficient solar energy conversion systems.[17,32,33] So far, very few thorough studies have been conducted on the junction itself in heterogeneous catalysts as well as on the nature of electronic transport properties, that is, the as-formed heterojunction barrier. In practice, classic semiconductor physics[34] illustrates that the current density through the Schottky junction is proportional to the possibility of the carriers overcoming the barrier at the interface and moving into the metal for catalytic reactions.[16]

Here, we construct a metal/semiconductor heterojunction catalyst system to provide further insight into the heterogeneous designs for an HER, which is composed of Pt nanoparticles (NPs) as highly active catalysts and PbS NCs with well-controlled shapes as light-harvesting material centers. We found that the photoenhanced electrocatalytic activities of the Pt/PbS catalyst are strongly dependent on the connecting junction between Pt and PbS. Experimental results show that the Pt/octahedral PbS NCs with Pt/PbS(111) junctions show the highest photoinduced enhancement of HER activity, which is ∼14.38 times higher than that of the Pt/cubic PbS NCs with the Pt/PbS(100) junction. This difference in photoinduced enhancement can be rationalized by the differences in the energy-barrier bending of the Pt/PbS Schottky junction due to the specific band structure and electron affinity. The calculations that are based on density functional theory (DFT) show that the electron affinity or ionization energy of PbS could be tuned by controlling the orientation and surface chemistry, indicating an effective way to manipulate the bending structure of the formed Pt/PbS Schottky junction. These results provide a good demonstration and guidance for the proper design and improvement of photocatalysis in various applications.

2. EXPERIMENTAL SECTION

2.1. Materials. Lead acetate trihydrate ($Pb(Ac)_2·3H_2O$, 99.99%; Aladdin), thioacetamide (TAA, 99.0%; Aladdin), hexadecyltrimethylammonium bromide (CTAB, 99.0%; Sinopharm), acetic acid (HAc, 99.5%; Sinopharm), isopropyl alcohol (IPA, 99.7%; Sinopharm), platinum (nominally 20% on carbon black; Alfa Aesar), sodium sulfide nonahydrate ($Na_2S·9H_2O$, 98.0%; Sinopharm), sodium sulfite anhydrous (Na_2SO_3, 97%; Sinopharm), and Nafion (Sigma) were used as received, without any further purification. Deionized water was produced using the Millipore Water Purification System (NANO pure; Billerica, MA; 18.2 MΩ).

2.2. Synthesis of PbS NCs. PbS NCs were synthesized according to a previously reported method[35] but with a little modification. In a typical synthesis of PbS octahedra, a 0.5 M TAA solution was first prepared. Next, 0.208 g of CTAB and 95.46 mL of deionized water were added to a 250 mL round-bottomed flask and then sonicated until dissolution of the surfactant. Thereafter, 0.521 mL of HAc and 0.861 g of $Pb(Ac)_2$ were added to the above solution one after the other and mixed at room temperature until complete dissolution. Finally, 4.54 mL of TAA solution (0.5 M) was added into the aqueous mixture of CTAB, HAc, and $Pb(Ac)_2$ at room temperature, and then, the mixture was heated to 80 °C for 24 h. Thus, the final concentrations of CTAB, HAc, $Pb(Ac)_2$, and TAA were 5.7, 91.0, 22.7, and 22.7 mM, respectively. On increasing the final TAA concentration, we obtain different shapes of PbS NCs. For PbS truncated octahedra or rhombicuboctahedra, 16 or 24 mL of TAA solution (0.5 M) was added into the aqueous mixture of CTAB, HAc, and $Pb(Ac)_2$ at room temperature. For PbS cubes, the only change was the use of 68.1 mL of TAA solution (1.0 M) in the synthesis, while keeping the other parameters the same. However, we have to make sure that the total solution volume is 100 mL for each experiment (the details are shown in Table S3). After the reaction, the black precipitates were purified by centrifugation and washed with water/IPA several times. The centrifuge used for precipitation was operated at 8000 rpm. Then, PbS powders were obtained after drying in a vacuum drier at 60 °C.

2.3. Fabrication of Pt/PbS Catalysts. To help improve the conductivity and dispersion of active catalysts, a carbon substrate was introduced. Four types of catalysts were tested for the HER, including different shapes of PbS NCs with the same amount of Pt loading (the weight ratio of Pt/PbS is 1:5). The Pt/PbS electrodes were prepared by the following steps. First, 10 mg of PbS powder mixed with 10 mg of Pt/C (20 wt %; Alfa Aesar) was dispersed in a 5 mL IPA solution and sonicated for several hours. Then, 50 μL of the above catalyst dispersion was loaded onto a glassy carbon electrode and naturally dried. Finally, 20 μL of a Nafion IPA solution (prepared with 25 μL of Nafion dispersed in 5 mL of IPA) was loaded onto each of the above electrodes to avoid sample stripping during testing.

2.4. Characterization. The morphology of the synthesized PbS NCs was examined by field-emission scanning electron microscopy (SEM; FEI Sirion 200, 5 kV) and transmission electron microscopy (TEM; JEM-2100F). Optical absorption spectra of the samples in the range of 200−1300 nm were recorded using a UV−vis−near IR spectrometer (750S; PerkinElmer). The crystalline phase was studied by X-ray diffraction (XRD; Rigaku, Ultima IV) analysis using Cu Kα radiation, with a scan speed of 10° min^{-1} ranging from 10 to 90°. Inductively coupled plasma atomic emission spectroscopy (ICP-AES) measurements were performed using a Thermo Scientific iCAP7600 Radial model. PbS powder was digested completely with nitric acid and diluted with 18 MΩ of water to obtain 1000 mL of clear solution for ICP-AES measurements.

2.5. Evaluation of HER Performance. The HER properties are studied using an electrochemical workstation (CHI760E) with a three-electrode system in a mixed electrolyte solution of Na_2S (0.25 M) and Na_2SO_3 (0.35 M) at room temperature, with a hydrogen electrode (HydroFlex) as the reference electrode, platinum foil as the counter electrode, and a rotating disk glassy carbon electrode as the working electrode. Argon was bubbled for 30 min before testing to avoid the presence of oxygen (electron acceptor) in the solution. A green laser beam (VA-I-N-532, 532 nm; Bangshou Corp, Beijing), with a diameter of 3 mm, was employed to perpendicularly illuminate the working electrodes during the measurements, and the illumination intensity was measured to be ∼3 W. Linear sweep voltammetry was conducted at a scan rate of 0.1 V s^{-1} at a rotation of 1600 rpm with and without illumination. $I-t$ curves were recorded at −0.2 V.

3. RESULTS AND DISCUSSION

To synthesize PbS NCs with different shapes, we adopted a water-phase synthetic method using CTAB as the surfactant, with an aqueous solution of lead acetate ($Pb(Ac)_2$) and TAA as the lead precursor and sulfur source, respectively.[35] Representative SEM and TEM images of the samples synthesized with different TAA concentrations are shown in Figure 1. In a typical synthesis, at lower TAA concentrations (e.g., 22.7 mmol L^{-1}) only octahedral PbS NCs were obtained (Figure 1a,b). Figure 1a shows that most of the obtained PbS NCs appear to be octahedral. Figure 1b indicates that the edge length of the octahedral NCs was about 40 nm and the inset gives the corresponding three-dimensional schematic illustration of an octahedron bound with (111) facets. With an increase in the TAA concentration, the PbS NCs gradually changed in shape from octahedrons to truncated octahedra and eventually into cubes. As shown in Figure 1c,d, when the TAA concentration

DOI: 10.1021/acsami.7b01428
ACS Appl. Mater. Interfaces 2017, 9, 12494−12500

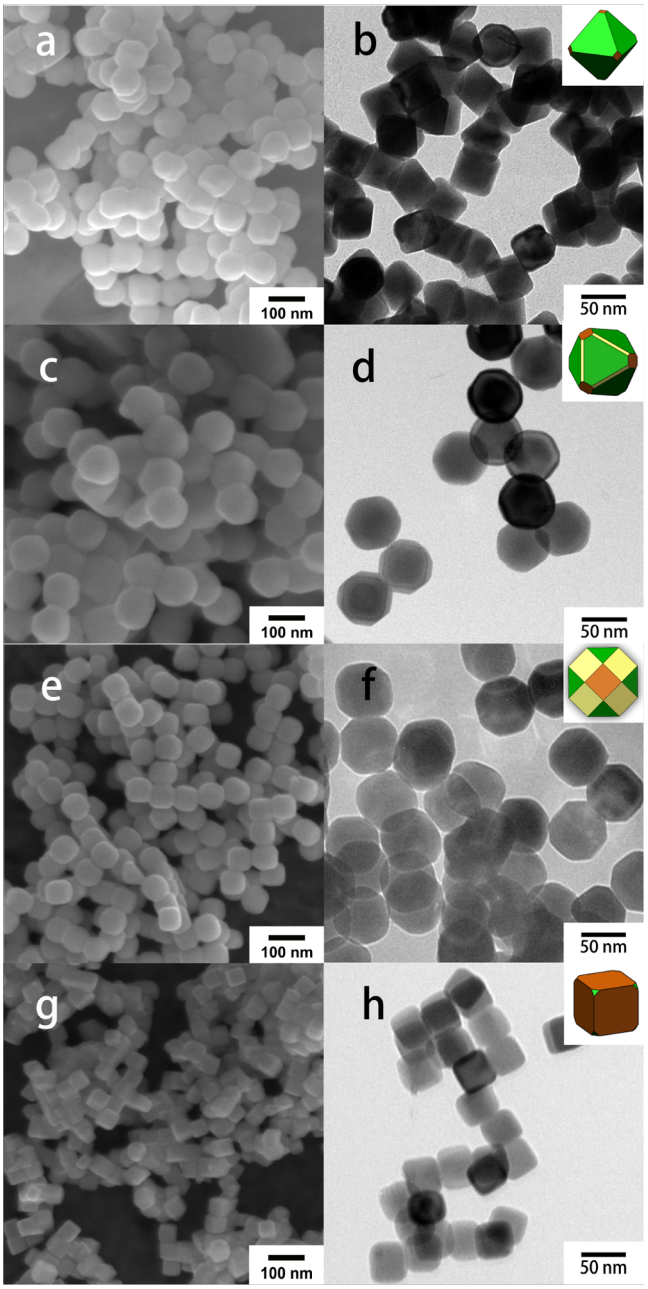

Figure 1. SEM (a, c, e, g) and TEM (b, d, f, h) images of PbS NCs prepared with TAA concentrations of 22.7 mM (a, b), 80 mM (c, d), 120 mM (e, f), and 681 mM (g, h). Insets are the corresponding models of an octahedron (b), a truncated octahedron (d), a rhombicuboctahedron (f), and a cube (h).

increased to 80 mM, monodispersed truncated octahedra enclosed with six (100) facets and eight (111) facets were obtained, and the higher the TAA concentration used, the larger the proportion of (100) facets (Figure 1d,f). It is worth noting that a small proportion of (110) facets existed on increasing the TAA concentration, as shown in the insets of Figure 1d,f. Despite this shape evolution, the PbS NCs remained ~40 nm in diameter, if measured in terms of the distance between the two edges. Further increasing the TAA concentration to 681 mM leads to the formation of 40 nm PbS cubes with nearly all (100) facets, which might have extremely small truncations at the corners.

We loaded the Pt NPs onto PbS NCs instead of onto carbon to construct a junction between Pt and PbS for transportation and utilization of photoelectrons. Figure S4 indicates that the PbS NCs have been successfully deposited with Pt NPs. It is clear that the small darker spherical particles are associated with Pt NPs, which have a narrow distribution of diameter, ranging from 2 to 3 nm. The Pt NPs were highly and uniformly dispersed on the surfaces of the PbS NCs. Both Pt and PdS preserved their original morphologies.

The HER performance of the Pt/PbS composite catalyst has been investigated in a three-electrode system. As shown in Figure 2a, the current densities of the Pt/PbS catalysts were measured over a potential range of −0.3 to 0 V (versus the reversible hydrogen electrode (RHE)) under 532 nm (~95.5 W cm^{-2}) illumination. The octahedral PbS NCs show the highest catalytic performance of ~13.7 mA cm^{-2} at −0.2 V after loading the same amount of Pt NPs. On combining different shapes of PbS NCs, all of the samples exhibit very different HER performances as well as photoinduced enhancements, which can probably be attributed to the different amounts of extra electrons transferred from the PbS to Pt surfaces under laser illumination because the light absorption of the junction formed between Pt and PbS is almost the same at 532 nm (please see the UV−vis spectra in Figure S5).

It is worth mentioning that Pt/PbS NCs with different shapes have different current densities even under dark conditions (see Figure S6) and the PbS(111) surface of the Pt NPs shows the best catalytic performance among that of all four surfaces. This result is probably attributed to the different interface contacts between Pt and PbS, which constitute the Schottky barriers with different heights that further influence the electron transportation between Pt and PbS as well as the consequent catalytic activity.[36]

Besides, current density−time (I−t) curves of Pt/PbS NCs with different shapes were also obtained under chopped illumination with a 532 nm laser at an interval of 30 s on/off at −0.2 V (Figure 2b). The Pt/PbS octahedral NCs show the highest photoinduced enhancement of HER activity (5.531 mA cm^{-2}), which is almost about 4.87 and 1.64 times higher than that of Pt on PbS rhombicuboctahedra and truncated octahedra (as shown in Table S1), respectively. The Pt/PbS cubic NCs show very little photoinduced enhancement during the on/off illumination sequence. In addition, the rapid transient response of current during the switch between the light-on and light-off statuses (Figure 2b) implies a well-formed junction contact between Pt NPs and PbS NCs.[37,38] In fact, the Pt/PbS NCs exhibited a high dependence of catalytic properties on the PbS contacting facet at the interface. As displayed in Figure 2c, the Pt/PbS NCs with almost all (111) planes showed the highest HER activity of 13.70 mA cm^{-2} and the highest photoinduced enhancement of 5.531 mA cm^{-2}. With a decrease in the percentage of (111), the enhancement of photocurrent also declined to different extents. This photoinduced enhancement of the Pt/PbS octahedron is ~14.38 times higher than that of the Pt/PbS cube (0.384 mA cm^{-2}). Therefore, on the basis of our experimental results, it can be concluded that the junction between the Pt and PbS surfaces plays a decisive role in the photoinduced HER activity.

To further explore the inherence between the atomic orientation of the junction and the photocatalytic properties of Pt/PbS NC composite photocatalysts, we built the atomic arrangement of a Pt/PbS NC junction to predict the junction barriers between Pt and PbS and study the optoelectronic

DOI: 10.1021/acsami.7b01428
ACS Appl. Mater. Interfaces 2017, 9, 12494−12500

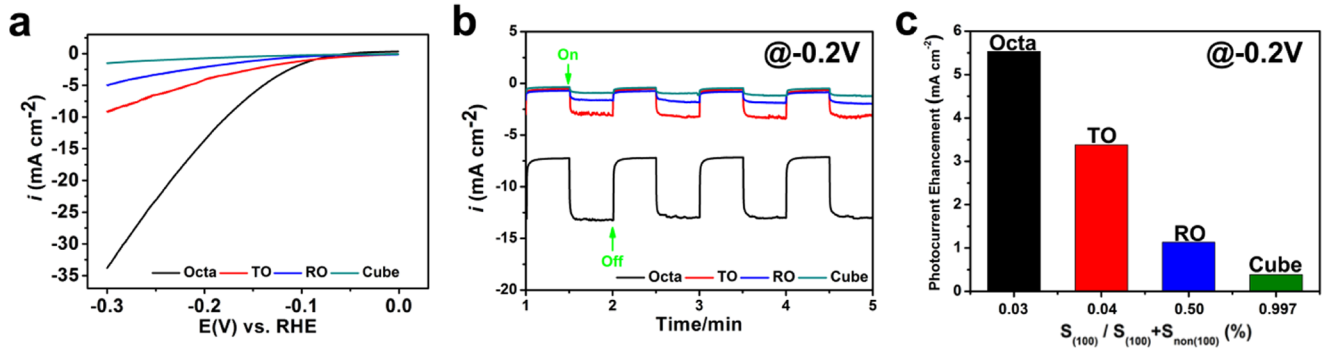

Figure 2. Photocatalytic performances of the Pt/PbS catalysts with different morphologies of PbS NCs for the HER process. (a) *I*−*V* curves of various Pt/PbS samples with 532 nm laser illuminations. (b) Photocurrent densities of various Pt/PbS samples under 532 nm laser illumination at a potential of −0.2 V (vs RHE). (c) Photoinduced HER enhancement of Pt/PbS samples with different facet proportions.

properties of Pt/PbS surfaces according to different atom and/or bond densities.

Figure S10 shows the side view of the Schottky junction between Pt and different PbS surfaces. The PbS(111) surface exhibits hexagonal close-packing whereas the PbS(100) surface presents a square close-packing. Thus, for PbS NCs, the (111) planes are more closely packed than the (100) planes. Thus, this suggests that the intrinsic surface energy of the (111) plane is higher than that of the (100) plane due to the high packing density.[39]

In fact, without consideration of the existence of surface states and with the assumption that all atoms in a PbS lattice are ionized, a higher surface atomic density on PbS(111) means a higher surface energy,[40] which indicates that the PbS(100)-terminated surface is generally energetically more favored compared with the (111) surface. Adopting a similar approach to that used before for work-function determinations,[41] we calculated the ionization energy of PbS, as schematically shown in Figure S9. Spin−orbit coupling is not used here for all surface calculations, and from the PbS(100)-terminated slab calculations, we find that the ionization energies with and without spin−orbit coupling are 4.21 and 4.29 eV, respectively. Thus, standard spin-polarized calculations have been performed for all of the other surfaces. The ionization energies for PbS with different terminations are studied and summarized in Figure 3a−c. We find that the ionization energy for the stable surface termination under a low sulfur condition, that is, the Pb(111)-terminated surface, is 4.11 eV, which is slightly lower than that of the stable surface termination under a higher sulfur chemical potential condition, that is, the PbS(100)-terminated surface. However, considering the adsorption of TAA, a more likely configuration of the polar Pb(111)-terminated surface is one with some sulfur adsorption. In other words, not a perfect Pb-terminated (111) surface but somewhere between a Pb-terminated and partially S-terminated (111) surface is more likely to be present in our synthesized PbS at a low TAA concentration, with the ionization energy of the (111) surface being larger than 4.11 eV (Figure 3b). On the other hand, a PbS(100)-terminated surface might have some sulfur vacancies, considering that the synthesized PbS are of the *n*-type and may contain S vacancies. Moreover, our simulations indicate that the formation energy for an S vacancy on the PbS(100)-terminated surface is smaller than that for a surface Pb vacancy (see the Supporting Information for more details). Thus, the ionization energy of the (111) and (100) surfaces formed in our experiment is likely to have the values indicated by the dashed arrows in Figure 3a,b, which means that the (111) surface is more likely to have a higher ionization energy and electron affinity energy under a low sulfur concentration compared to those of a (100) surface. Consequently, the work function of PbS(111) should be larger than that of PbS(100). The DFT calculation shows that at a low sulfur chemical potential the Pb(111)-terminated surface would be stabilized, and this result also agrees with our experimental observation that the fraction of the (111) surface is higher for a low TAA concentration. We have also calculated the ionization energy for nonpolar PbS(110) with a higher surface energy. Similar to the PbS(100) surface, the PbS(110) surface is likely to have a sulfur vacancy and hence shows a similar ionization energy to that of a PbS(111) surface (Figure 3c, see the details of the calculation in the Supporting Information).

On the basis of the calculated work functions of (100), (111), and (110), Figure 3d schematically illustrates the proposed band edge energy diagram of the PbS (100), (111), and (110) planes before equilibration of the Fermi levels at the Pt/PbS interface, respectively. Because the work function of Pt is larger than that of an n-type PbS semiconductor, we could observe that the PbS energy band edges bend upward toward the Pt surface after Fermi-level alignment due to electron transfer from the Pt NPs to the PbS NCs. Because the (111)/(110) planes have more negative valence band and conduction band energies than those of the (100) planes, as shown in Figure 3d, the obtained upward band bending of the (111)/(110) planes becomes less steep, as shown in Figure 3e. In fact, upon equilibration of the Fermi levels at the Pt/PbS interface, a space−charge region forms on the semiconductor surface and therefore the metal−semiconductor Schottky junction forms a barrier for electrons and holes due to the upward band bending. In Figure 3e, the barrier height is obtained from the following equation:[42]

$$qV_D = W_m - W_s \quad (1)$$

where V_D is the contact potential difference on the side of semiconductor PbS, W_m is the work function of the metal Pt, and W_s is the work function of the semiconductor PbS.

Because the work function of the (111)/(110) plane should be larger than that of the (100) plane, as discussed above, upon coupling Pt with PbS, different exposed facets could cause different barrier heights and therefore different degrees of bending. The band bending becomes less steep with the formation of a Schottky contact between Pt and PbS(111)/(110), as shown in Figure 3e. The less steep the upward

DOI: 10.1021/acsami.7b01428
ACS Appl. Mater. Interfaces 2017, 9, 12494−12500

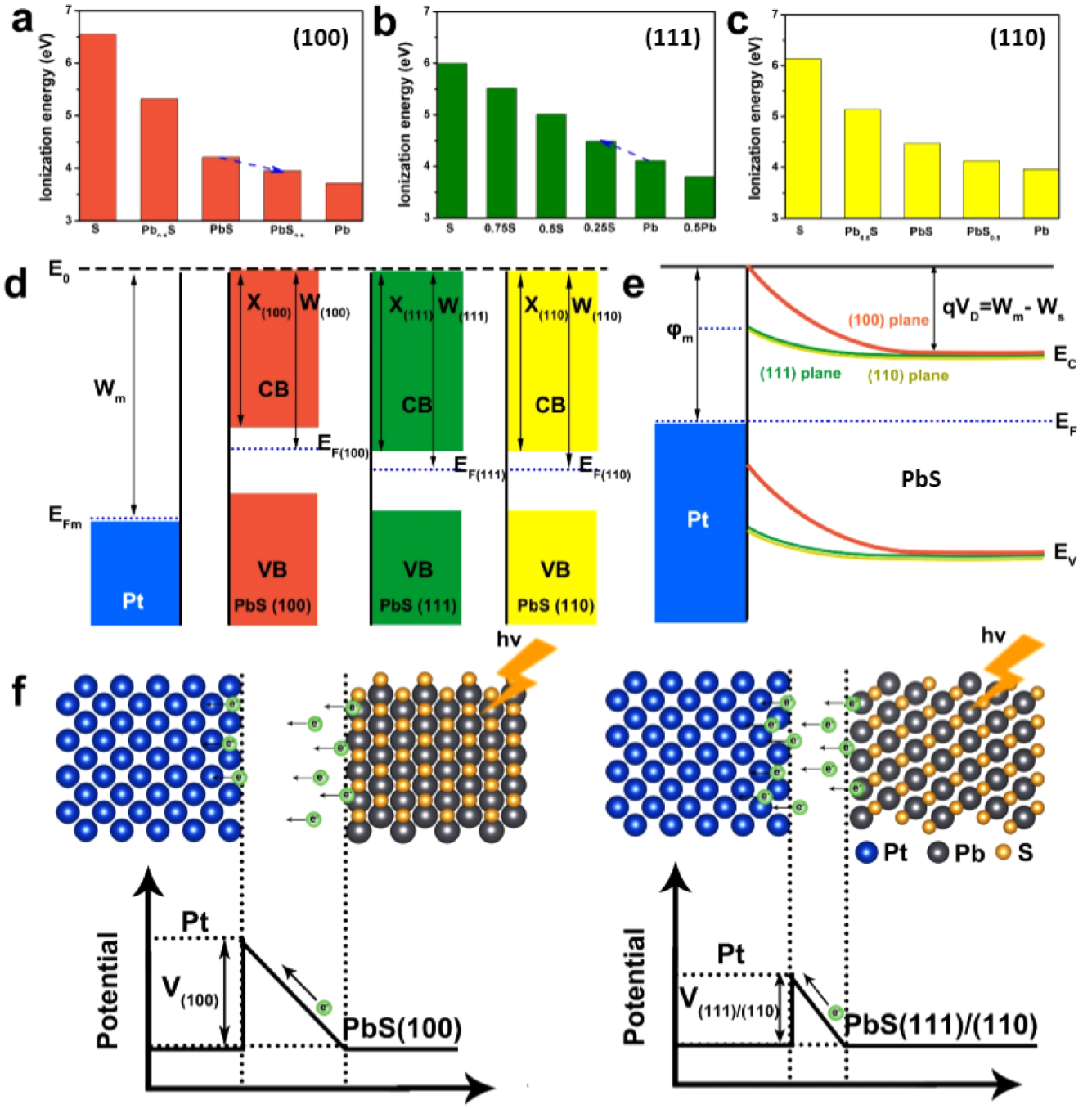

Figure 3. (a–c) Ionization energies of the (100), (111), and (110) surfaces of PbS with different surface terminations, respectively. The dashed arrows represent the probable range of ionization energies of PbS with different orientations in our experiment. (d–e) Schematic representations of the energy band diagram for the Schottky junction before and after the equilibration of Fermi levels at the Pt/PbS interface. The appearance of (111)/(110) close-packed planes induces lower band bending, just as represented by the green and yellow curves in Figure 1e. (f) Schematic illustration of electron transfer through Pt/PbS junctions.

bending, the easier it is for the electrons to escape from the surface of the semiconductor (Figure 3f). For the (111)/(110) plane, there are more photogenerated electrons that overcome the energy barrier and then transfer to the Pt surface under illumination, which is reflected by the photocurrent in Figure 2.

Theoretically, the current density through a Schottky junction is proportional to the possibility, P, that the carriers overcome the barrier and arrive at the metal[34]

$$J_k \propto P = \exp\left[-\frac{4\pi}{h}\left(\frac{m_n^* \varepsilon_r \varepsilon_0}{N_D}\right)^{1/2}(V_D - V)\right] \quad (2)$$

where J_k is the current density through Pt; h is Planck's constant; m_n^* is the effective mass of the electron; ε_r is the dielectric constant of PbS; ε_0 is the dielectric constant in vacuum, that is, 8.85×10^{-12} F m^{-1}; and N_D is the doping concentration of PbS. Typically, the m_n^* of PbS is equal to $0.11m_0$ (m_0 is the mass of the electrons), the ε_r of PbS[34] is 169,

DOI: 10.1021/acsami.7b01428
ACS Appl. Mater. Interfaces 2017, 9, 12494–12500

and N_D is calculated from the ICP-AES results and atom figurations (i.e., calculate the ratio of excess Pb atoms to a perfect PbS lattice with a certain plane exposed).

Then, the enhancement ratio, $\frac{J_{k,(111)}}{J_{k,(100)}} = \exp\left[\frac{4\pi}{h}\left(\frac{m_n^* \varepsilon_r \varepsilon_0}{N_D}\right)^{1/2} \Delta V_D\right]$, is exponentially related to the difference between the two Schottky barrier heights. The larger the ΔV_D value, the larger the enhancement ratio obtained.

In fact, the photoinduced enhancement of Pt/PbS octahedra is ∼14.38 times higher than that of Pt/PbS cubes, which indicates that ΔV_D is likely to be 0.23 V and the sulfur concentration on the (111) surface is likely to be 12% according to DFT calculations, although it is difficult to measure the amount of sulfur decorated on the PbS surface.

As a result, controlling the contacting interfaces of the metal/semiconductor materials is an effective method to modulate the formed Schottky barrier height and then construct the desired heterojunction for optimizing the catalytic performance. As shown in Figure 3f, such a band-bending configuration could be achieved by tuning the ionization energy of PbS NCs, that is, through control of the surface orientation and/or surface termination of PbS. The experiment and calculations indicate that the PbS(100) surface will have a smaller ionization energy at a low sulfur concentration and hence display a larger band bending when forming an interfacial contact with Pt.

4. CONCLUSIONS

In summary, we have designed a desired Pt/PbS heterojunction for optimizing the HER photocatalytic performance through manipulation of the interfacial barrier bending. We have discussed the effect of the as-formed heterojunction barrier on the photocatalytic performance of the Pt/PbS composite catalyst system from a perspective of electron-transport properties at the junction. By controlling the exposed PbS facets at the interface, we can obtain Pt/PbS composite catalysts with different barrier bendings at the junction. The experimental results show that the Pt/octahedral PbS NCs with PbS(111) facets show the highest photoinduced enhancement of HER activity, which is ∼14.38 times higher than that of the PbS NCs with only PbS(100) facets. Modulation of the Schottky barrier height by controlling the exposed facets may offer a promising approach to construct the desired heterojunction for optimizing the catalytic performance and even control the catalytic activity of the metal−semiconductor system through regulation of the energy band structure, which may play a significant role in improvement of the catalytic performance in the future.

■ ASSOCIATED CONTENT

Supporting Information

The Supporting Information is available free of charge on the ACS Publications website at DOI: 10.1021/acsami.7b01428.

Computed band structure of bulk PbS, XRD patterns, TEM images of the Pt/PbS composite catalysts, UV−vis absorption spectrum, $I-V$ curves of different Pt/PbS samples with and without 532 nm laser illumination, photoinduced enhancement during the on/off illumination sequence and the corresponding HER activity of different-shaped PbS when loading Pt NPs under illumination, ICP analysis of the composition of PbS NCs, FTIR spectra, crystal plane ratio of (100) of the synthesized PbS NCs as a function of the TAA concentration used, planar averaged electrostatic potential as a function of the position in the slab model, and schematics for the surface atom array of the synthesized PbS and Pt junction (PDF)

■ AUTHOR INFORMATION

Corresponding Authors

*E-mail: hong.zhu@sjtu.edu.cn (H.Z.).
*E-mail: dengtao@sjtu.edu.cn (T.D.).
*E-mail: jianbowu@sjtu.edu.cn (J.W.).

ORCID

Jianbo Wu: 0000-0002-3574-5585

Author Contributions

§Y.L. and X.G. contributed to this work equally.

Notes

The authors declare no competing financial interest.

■ ACKNOWLEDGMENTS

This work is sponsored by the thousand talents program for distinguished young scholars from the Chinese Government, the National Science Foundation of China (51521004 and 51420105009), the start-up fund (J.W.), and the Zhi-Yuan Endowed fund (T.D.) from Shanghai Jiao Tong University. H.Z. acknowledges the support of the Shanghai Sailing Program (16YF1406000).

■ REFERENCES

(1) Morales-Guio, C. G.; Tilley, S. D.; Vrubel, H.; Grätzel, M.; Hu, X. Hydrogen Evolution from a Copper (I) Oxide Photocathode Coated with an Amorphous Molybdenum Sulphide Catalyst. *Nat. Commun.* **2014**, *5*, 3059−3065.

(2) Popczun, E. J.; Read, C. G.; Roske, C. W.; Lewis, N. S.; Schaak, R. E. Highly Active Electrocatalysis of the Hydrogen Evolution Reaction by Cobalt Phosphide Nanoparticles. *Angew. Chem.* **2014**, *126*, 5531−5534.

(3) Li, Y.; Wang, H.; Xie, L.; Liang, Y.; Hong, G.; Dai, H. MoS_2 Nanoparticles Grown on Graphene: An Advanced Catalyst for the Hydrogen Evolution Reaction. *J. Am. Chem. Soc.* **2011**, *133*, 7296−7299.

(4) Mazumder, V.; Lee, Y.; Sun, S. Recent Development of Active Nanoparticle Catalysts for Fuel Cell Reactions. *Adv. Funct. Mater.* **2010**, *20*, 1224−1231.

(5) Hsu, I. J.; Kimmel, Y. C.; Jiang, X.; Willis, B. G.; Chen, J. G. Atomic Layer Deposition Synthesis of Platinum−Tungsten Carbide Core−Shell Catalysts for the Hydrogen Evolution Reaction. *Chem. Commun.* **2012**, *48*, 1063−1065.

(6) Long, N. V.; Yang, Y.; Thi, C. M.; Van Minh, N.; Cao, Y.; Nogami, M. The Development of Mixture, Alloy, and Core-Shell Nanocatalysts with Nanomaterial Supports for Energy Conversion in Low-Temperature Fuel Cells. *Nano Energy* **2013**, *2*, 636−676.

(7) Qi, Y.; Wu, J.; Zhang, H.; Jiang, Y.; Jin, C.; Fu, M.; Yang, H.; Yang, D. Facile Synthesis of Rh−Pd Alloy Nanodendrites as Highly Active and Durable Electrocatalysts for Oxygen Reduction Reaction. *Nanoscale* **2014**, *6*, 7012−7018.

(8) Lv, H.; Xi, Z.; Chen, Z.; Guo, S.; Yu, Y.; Zhu, W.; Li, Q.; Zhang, X.; Pan, M.; Lu, G.; et al. A New Core/Shell NiAu/Au Nanoparticle Catalyst with Pt-like Activity for Hydrogen Evolution Reaction. *J. Am. Chem. Soc.* **2015**, *137*, 5859−5862.

(9) Wang, X.; Su, R.; Aslan, H.; Kibsgaard, J.; Wendt, S.; Meng, L.; Dong, M.; Huang, Y.; Besenbacher, F. Tweaking the Composition of NiMoZn Alloy Electrocatalyst for Enhanced Hydrogen Evolution Reaction Performance. *Nano Energy* **2015**, *12*, 9−18.

(10) Du, N.; Wang, C.; Wang, X.; Lin, Y.; Jiang, J.; Xiong, Y. Trimetallic TriStar Nanostructures: Tuning Electronic and Surface

DOI: 10.1021/acsami.7b01428
ACS Appl. Mater. Interfaces 2017, 9, 12494−12500

Structures for Enhanced Electrocatalytic Hydrogen Evolution. *Adv. Mater.* **2016**, *28*, 2077−2084.
(11) Yang, T.; Zhu, H.; Wan, M.; Dong, L.; Zhang, M.; Du, M. Highly Efficient and Durable PtCo Alloy Nanoparticles Encapsulated in Carbon Nanofibers for Electrochemical Hydrogen Generation. *Chem. Commun.* **2016**, *52*, 990−993.
(12) Peng, Z.; Wu, J.; Yang, H. Synthesis and Oxygen Reduction Electrocatalytic Property of Platinum Hollow and Platinum-on-Silver Nanoparticles. *Chem. Mater.* **2010**, *22*, 1098−1106.
(13) Wu, J.; Li, P.; Pan, Y.-T.; Warren, S.; Yin, X.; Yang, H. Surface Lattice-Engineered Bimetallic Nanoparticles and their Catalytic Properties. *Chem. Soc. Rev.* **2012**, *41*, 8066−8074.
(14) Wang, D.-Y.; Gong, M.; Chou, H.-L.; Pan, C.-J.; Chen, H.-A.; Wu, Y.; Lin, M.-C.; Guan, M.; Yang, J.; Chen, C.-W.; et al. Highly Active and Stable Hybrid Catalyst of Cobalt-Doped FeS_2 Nanosheets−Carbon Nanotubes for Hydrogen Evolution Reaction. *J. Am. Chem. Soc.* **2015**, *137*, 1587−1592.
(15) Kudo, A.; Miseki, Y. Heterogeneous Photocatalyst Materials for Water Splitting. *Chem. Soc. Rev.* **2009**, *38*, 253−278.
(16) Zhang, Z.; Yates, J. T., Jr. Band Bending in Semiconductors: Chemical and Physical Consequences at Surfaces and Interfaces. *Chem. Rev.* **2012**, *112*, 5520−5551.
(17) Li, R.; Zhang, F.; Wang, D.; Yang, J.; Li, M.; Zhu, J.; Zhou, X.; Han, H.; Li, C. Spatial Separation of Photogenerated Electrons and Holes among {010} and {110} Crystal Facets of $BiVO_4$. *Nat. Commun.* **2013**, *4*, 1432−1438.
(18) Zhou, X.; Lan, J.; Liu, G.; Deng, K.; Yang, Y.; Nie, G.; Yu, J.; Zhi, L. Facet-Mediated Photodegradation of Organic Dye over Hematite Architectures by Visible Light. *Angew. Chem.* **2012**, *124*, 182−186.
(19) Bi, Y.; Ouyang, S.; Umezawa, N.; Cao, J.; Ye, J. Facet Effect of Single-Crystalline Ag_3PO_4 Sub-Microcrystals on Photocatalytic Properties. *J. Am. Chem. Soc.* **2011**, *133*, 6490−6492.
(20) Xi, G.; Ye, J. Synthesis of Bismuth Vanadate Nanoplates with Exposed {001} Facets and Enhanced Visible-Light Photocatalytic Properties. *Chem. Commun.* **2010**, *46*, 1893−1895.
(21) Peng, Z.; You, H.; Wu, J.; Yang, H. Electrochemical Synthesis and Catalytic Property of Sub-10 nm Platinum Cubic Nanoboxes. *Nano Lett.* **2010**, *10*, 1492−1496.
(22) Wu, J.; Zhang, J.; Peng, Z.; Yang, S.; Wagner, F. T.; Yang, H. Truncated Octahedral Pt_3Ni Oxygen Reduction Reaction Electrocatalysts. *J. Am. Chem. Soc.* **2010**, *132*, 4984−4985.
(23) Wu, J.; Gross, A.; Yang, H. Shape and Composition-Controlled Platinum Alloy Nanocrystals using Carbon Monoxide as Reducing Agent. *Nano Lett.* **2011**, *11*, 798−802.
(24) Wu, J.; Qi, L.; You, H.; Gross, A.; Li, J.; Yang, H. Icosahedral Platinum Alloy Nanocrystals with Enhanced Electrocatalytic Activities. *J. Am. Chem. Soc.* **2012**, *134*, 11880−11883.
(25) Wu, J.; Yang, H. Platinum-based Oxygen Reduction Electrocatalysts. *Acc. Chem. Res.* **2013**, *46*, 1848−1857.
(26) Collins, G.; Schmidt, M.; O'Dwyer, C.; McGlacken, G.; Holmes, J. D. Enhanced Catalytic Activity of High-Index Faceted Palladium Nanoparticles in Suzuki−Miyaura Coupling Due to Efficient Leaching Mechanism. *ACS Catal.* **2014**, *4*, 3105−3111.
(27) Xiao, X.; Liu, X.; Zhao, H.; Chen, D.; Liu, F.; Xiang, J.; Hu, Z.; Li, Y. Facile Shape Control of Co_3O_4 and the Effect of the Crystal Plane on Electrochemical Performance. *Adv. Mater.* **2012**, *24*, 5762−5766.
(28) Tan, C. S.; Chen, H. S.; Chiu, C. Y.; Wu, S. C.; Chen, L. J.; Huang, M. H. Facet-Dependent Electrical Conductivity Properties of PbS Nanocrystals. *Chem. Mater.* **2016**, *28*, 1574−1580.
(29) Yuan, G.-Z.; Hsia, C.-F.; Lin, Z.-W.; Chiang, C.; Chiang, Y.-W.; Huang, M. H. Highly Facet-Dependent Photocatalytic Properties of Cu2O Crystals Established through the Formation of Au-Decorated Cu2O Heterostructures. *Chem. − Eur. J.* **2016**, *22*, 12548−12556.
(30) Tan, C.-S.; Chen, Y.-J.; Hsia, C.-F.; Huang, M. H. Facet-Dependent Electrical Conductivity Properties of Silver Oxide Crystals. *Chem. − Asian J.* **2017**, *12*, 293−297.
(31) Wu, S.-C.; Tan, C.-S.; Huang, M. H. Strong Facet Effects on Interfacial Charge Transfer Revealed through the Examination of Photocatalytic Activities of Various Cu2O−ZnO Heterostructures. *Adv. Funct. Mater.* **2017**, *27*, No. 1604635.
(32) Li, R.; Han, H.; Zhang, F.; Wang, D.; Li, C. Highly Efficient Photocatalysts Constructed by Rational Assembly of Dual-Cocatalysts Separately on Different Facets of $BiVO_4$. *Energy Environ. Sci.* **2014**, *7*, 1369−1376.
(33) Zhu, J.; Fan, F.; Chen, R.; An, H.; Feng, Z.; Li, C. Direct Imaging of Highly Anisotropic Photogenerated Charge Separations on Different Facets of a Single $BiVO_4$ Photocatalyst. *Angew. Chem.* **2015**, *127*, 9239−9242.
(34) Sze, S.; Kwok, K. N. *Physics of Semiconductor Devices*, 3rd ed.; Wiley: Hoboken, NJ, 2007.
(35) Zhao, Z.; Zhang, K.; Zhang, J.; Yang, K.; He, C.; Dong, F.; Yang, B. Synthesis of Size and Shape Controlled PbS Nanocrystals and their Self-Assembly. *Colloids Surf., A* **2010**, *355*, 114−120.
(36) Crowell, C. R.; Sze, S. M. Current Transport in Metal-Semiconductor Barriers. *Solid-State Electron.* **1966**, *9*, 1035−1048.
(37) Kang, Q.; Cao, J.; Zhang, Y.; Liu, L.; Xu, H.; Ye, J. Reduced TiO_2 Nanotube Arrays for Photoelectrochemical Water Splitting. *J. Mater. Chem. A* **2013**, *1*, 5766−5774.
(38) Xie, C.; Li, F.; Zeng, L.; Luo, L.; Wang, L.; Wu, C.; Jie, J. Surface Charge Transfer Induced p-CdS Nanoribbon/n-Si Heterojunctions as Fast-Speed Self-Driven Photodetectors. *J. Mater. Chem. C* **2015**, *3*, 6307−6313.
(39) Zhao, N.; Qi, L. Low-Temperature Synthesis of Star-Shaped PbS Nanocrystals in Aqueous Solutions of Mixed Cationic/Anionic Surfactants. *Adv. Mater.* **2006**, *18*, 359−362.
(40) Zhou, Z. Y.; Tian, N.; Li, J. T.; Broadwell, I.; Sun, S. G. Nanomaterials of High Surface Energy with Exceptional Properties in Catalysis and Energy Storage. *Chem. Soc. Rev.* **2011**, *40*, 4167−4185.
(41) Zhu, H.; Aindow, M.; Ramprasad, R. Stability and Work Function of TiC_xN_{1-x} Alloy Surfaces: Density Functional Theory Calculations. *Phys. Rev. B: Condens. Matter Mater. Phys.* **2009**, *80*, No. 201406(R).
(42) Bardeen, J. Surface States and Rectification at a Metal-Semiconductor Interface. *Phys. Rev.* **1947**, *71*, 717−727.

DOI: 10.1021/acsami.7b01428
ACS Appl. Mater. Interfaces 2017, 9, 12494−12500